ROYAL SOCIETY
OF CHEMISTRY

PAPER

Check for updates

Highly efficient and selective *Maerua subcordata* tuber-derived activated carbons for enhanced removal of methylene blue from wastewater samples

Addis Mekonnen Woldehana,[a] Amare Aregahegn Dubale, [ID] *[b]
Andualem Mekonnen Hiruy[a] and Muzammil Anjum [ID] [c]

The discharge of methylene blue dye from textile and pharmaceutical industries increasingly threatens environmental safety and human health by introducing toxic contaminants. Because of the high cost of commercial activated carbon and the limited efficiency of many alternative adsorbents, the development of efficient and cost-effective materials remains highly desirable. In this study, the AC derived from *Maerua subcordata* tuber (MS-AC) was prepared using a simple and scalable method involving Na_2CO_3 activation followed by thermal treatment. The elemental composition, structural features, and morphology of the prepared MS-AC were examined using XPS, FTIR spectroscopy, XRD, SEM, and SEM/EDX elemental mapping. XRD, SEM, and FTIR spectroscopic analyses confirmed the enhanced amorphous structure, high porosity, and enriched surface functional groups after Na_2CO_3 activation. Batch adsorption tests were performed to investigate the ideal conditions for MB adsorption on MS-AC. The adsorption behavior followed the Langmuir isotherm model, with a maximum adsorption capacity of 158.7 mg g^{-1} at 25 °C, which is superior to various materials reported earlier. The kinetic studies were best explained by the PSO model, while the Boyd model indicated film diffusion as the dominant rate-controlling step. Thermodynamic study disclosed negative ΔG° values, approving spontaneous adsorption, while a positive ΔH° value of 106.4 kJ mol^{-1} indicated an endothermic chemisorption process. MS-AC exhibited excellent selectivity toward MB in mixed-dye systems and remarkable stability, retaining over 90% removal efficiency after four adsorption–desorption cycles using ethanol. Furthermore, MS-AC achieved 96.7% MB removal from real wastewater samples. The adsorption mechanism is mainly ascribed to hydrogen bonding, π–π stacking interactions, and electrostatic interactions between the methylene blue molecules and the MS-AC surface.

1. Introduction

The health of all living beings, including humans, is seriously threatened by global environmental degradation, which includes the contamination of air, water, and soil.[1] Water pollution caused by dye effluents raises widespread concerns as these discharges enter water systems, leading to substantial ecological challenges.[2] Various industries such as textiles, pharmaceuticals, rubber, paper, leather, plastics, cosmetics, and printing use large quantities of synthetic dyes. Consequently, these industries also produce substantial volumes of effluents containing these dyes.[3] Industrial waste dyes can be either cationic or anionic. Commercial water containing more than 5 mg kg^{-1} of cationic dyes may be harmful to the environment and should not be consumed by humans or marine organisms.[4] Dyes have destructive effects on human health, environment, and natural water supplies. They are chemically stable and non-biodegradable, posing significant toxicological and carcinogenic risks.[5,6] Their chemical composition makes them highly noticeable and can lead to pollution and various problems.[7,8]

Methylene blue, a heterocyclic cationic dye with the chemical formula $C_{16}H_{18}N_3SCl$, is widely used in the textile industry, microbiological staining, fistula detection, and dermatological treatments.[9] However, it is non-biodegradable and resistant to conventional biological treatments, such as activated sludge and anaerobic digestion, leading to persistent environmental contamination.[10] Prolonged exposure to this

[a] *Center for Environmental Science, College of Natural and Computational Sciences, Addis Ababa University, 1176, Ethiopia*

[b] *Center for Material Science and Engineering, College of Natural and Computational Sciences, Addis Ababa University, 1176, Ethiopia.*
E-mail: amare.aregahegn@aau.edu.et

[c] *Institute of Soil and Environmental Sciences, Pir Mehr Ali Shah Arid Agriculture University, Shamsabad, Murree Rd, Rawalpindi 46300, Pakistan*

dye can result in various health effects, including nausea, vomiting, diarrhea, anemia, hypertension, and potential carcinogenic effects.[11–13] Eliminating colors from tainted wastewater is essential for reducing its harmful and unsightly effects on both humans and ecosystems.[14,15] Various conventional methods including chemical oxidation, coagulation, adsorption, photocatalytic degradation, and reverse osmosis have been widely used for the removal of dyes from wastewater samples.[16–19] Adsorption is considered as a superior alternative due to its simple design, ease of operation, lower initial cost, and resilience to toxic materials.[14,20]

Numerous porous adsorbents, such as organic clay chitosan composites and charcoal, are utilized for wastewater treatment. However, challenges including complex synthesis procedures, selective adsorption, and limited adsorption capacity persist. These issues have promoted research interest in exploring new materials to solve these problems.[21] Plant-based activated materials exhibit structural heterogeneity, comprising micropores, mesopores, and macropores, which enhance the accessibility of adsorbates.[22] Recent studies have explored bio-adsorbents from various sources including *Citrullus colocynthis* seeds,[23] banana peels,[24] apple peels,[25] *Rumex abyssinicus* leaves,[26] and *Tectona grandis* seed powder,[3] demonstrating the potential of natural biomaterials for the efficient removal of MB. *Maerua subcordata* is a wild shrub belonging to the Capparaceae family that grows in the arid and semi-arid regions of East Africa, including parts of southern Ethiopia inhabited by the Dasenech people.[27] After harvesting, the tubers are used by nearby communities as a natural coagulant for treating dirty water, and the enlarged roots of the plant enable regeneration, showcasing its eco-friendliness.[28] Chemical activation using agents such as KOH, H_3PO_4, and Na_2CO_3 enhances porosity, surface area, and adsorption efficiency through impregnation-carbonization processes.[29] Consequently, activating *Maerua subcordata* is expected to significantly improve its adsorption and wastewater treatment capacity. To date, the use of activated carbons derived from *Maerua subcordata* tubers as bio-adsorbents for dye removal has not been reported in the literature.

In this study, an activated *Maerua subcordata* adsorbent was prepared using a straightforward and scalable method that involved chemical activation followed by calcination. The main aim was to exploit the bio-adsorptive potential of activated MS tubers for the removal of MB dye from aqueous environments. The MS tuber powder was chemically activated with Na_2CO_3 to produce an effective adsorbent, which was subsequently characterized using XPS, FTIR spectroscopy, XRD, SEM, and SEM/EDX mapping. The effects of key operational parameters such as solution pH, contact time, initial dye concentration, adsorbent dosage, and temperature were systematically investigated and optimized. Furthermore, post-characterization, adsorption isotherm models, as well as kinetic and thermodynamic studies were conducted to clarify the adsorption mechanisms. Multiple regeneration and reuse cycles were performed to evaluate the reusability and stability of the adsorbent. Overall, this study enhances the broader application of *Maerua subcordata*-based adsorbents in environmental remediation by providing new insights into the development of activated bio-adsorbent materials.

2. Experimental

2.1. Chemicals and apparatus

The chemicals utilized in this study, including sodium carbonate (98%), methylene blue dye (95%), sodium hydroxide (98%), and hydrochloric acid (37%), were bought from Alfa Aesar. A methylene blue stock solution was prepared by diluting the standard MB solution with deionized water (DI). Sample weighing was performed using a digital balance (ESJ-200-4, Japan), a muffle furnace 6104 model was employed for calcination, and an oven (DHG-9070, Japan) was used for drying the materials. Different-sized (50–1000 mL) volumetric and conical flasks, Whatman filter paper (42.5 mm), and a systronic digital pH meter (model 802) were used for pH measurements. A Sohag orbital shaker incubator was also used. Micropipettes and volumetric flasks of appropriate sizes were employed to quantify the reagents and solution volumes. Analytical grade chemicals were used without further purification. The MB concentration in synthetic and real wastewater was quantified at 665 nm using a double-beam UV-visible spectrophotometer (UV-2900, Hitachi, Japan).

2.2. Preparation of the adsorbent before and after activation

The tubers of *Maerua subcordata* (5 kg) were collected from the South Omo district of the Omorate pastoral area in Ethiopia. The tubers were cleaned with deionized water, dried at 90 °C for 36 h, pulverized, and filtered (<300 μm). The finely powdered material was then stored for direct use as an adsorbent in subsequent experiments and for further activation. The finely powdered MS tubers were activated with sodium carbonate following the procedures reported in the literature.[30–32] Briefly, 8 g of sodium carbonate was dissolved in 380 mL of double-distilled water. Next, 4 g of ground MS tubers were soaked in this solution and stirred for 12 hours. The mixture was then filtered, and the residue was dried in an oven at 120 °C for at least 6 hours. The dried impregnated material was then carbonized at 400 °C in a muffle furnace for 90 min. After carbonization, the mixture was removed from the furnace and allowed to cool at ambient temperature. The pyrolyzed material was then washed four times with 5% HCl and then repeatedly washed with deionized water until a neutral pH was achieved. Finally, activated powder was taken into a vacuum oven set at 90 °C for 12 h, allowed to cool down at ambient temperature, and filtered through a 250 μm mesh. The as-prepared adsorbent before and after activation were labeled as RMS and MS-AC, respectively.

2.3. Characterization of the adsorbent

The prepared powders were analyzed by scanning electron microscopy (SEM), Fourier transform infrared (FTIR) spectroscopy, X-ray diffraction (XRD), energy-dispersive spectroscopy (EDS), UV-vis spectrophotometry, and X-ray photoelectron spectroscopy (XPS). To analyze the crystallinity of the samples,

XRD analysis was conducted using a Cu Kα radiation source at a λ value of 1.5406 Å. A NEXUS-670 FT-IR instrument was utilized to investigate the characteristic groups in the material. XPS and field emission-SEM were used to scrutinize the elemental composition and morphology of the as-produced adsorbents, respectively. A Malvern Zetasizer Nano ZS90 was used to measure the zeta potential of the adsorbent.

2.4. Batch experiments

In this study, various batch adsorption experiments were conducted using MS-AC as an adsorbent in 0.1 mL Erlenmeyer flasks. Initially, the pH of a solution comprising 75 mg of adsorbent and 50 mL of 100 mg L^{-1} MB was attuned to 2, 4, 6, 8, 10, and 12 using 0.1 M HCl and NaOH solutions. After that, the resulting combination was mixed for 40 minutes at 120 rpm and ambient temperature. Subsequently, 5 mL of the mixture was taken out, separated, and the clear solution was subjected to quantifying the MB content using a UV-vis machine at 665 nm. The effect of adsorbent dose, contact time, stirring speed, and initial concentration of MB was studied by varying these parameters from 15 to 115 mg, 10 to 110 min, 40 to 200 rpm, and 10 to 160 mg L^{-1}, respectively. The elimination capability of MB by RMS and MS-AC was evaluated using eqn (1):

$$\% \text{ Removal} = \frac{(C_0 - C_e)}{C_0} \times 100, \quad (1)$$

where C_e and C_0 are the equilibrium and the initial concentration of MB (mg L^{-1}), respectively. Furthermore, the adsorption capacity of MB on RMS and MS-AC was obtained employing eqn (2):

$$q_e = \frac{(C_0 - C_e)V}{m}, \quad (2)$$

where C_e and C_0 are the equilibrium and the initial concentration of MB (mg L^{-1}), respectively, and m and V stand for the mass of adsorbents (in grams) and the batch volume of MB (in liters), respectively.

2.5. Isotherm and kinetic studies

The adsorption performance was assessed using various isotherm models including Freundlich, Langmuir, Dubinin–Radushkevich, and Temkin models over an MB concentration ranging from 10 to 160 mg L^{-1} at 25 °C, pH 8, a stirring speed of 120 rpm, an adsorbent dosage of 75 mg, and a contact time of 40 minutes. The adsorption kinetics was evaluated using the Boyd, pseudo-second-order, pseudo-first-order, and intraparticle diffusion models based on MB uptake at various times of interactions. The calculated results for the isotherm and kinetic analysis are provided in the SI.

2.6. Thermodynamic studies

The dependency of MB sorption on temperature using MS-AC was investigated by varying its value from 298 to 313 K. The thermodynamic parameters were calculated employing eqn (3) and (4):

$$\Delta G^0 = -RT \ln K_T, \quad (3)$$

$$\ln K_T = \frac{\Delta S^0}{R} - \frac{\Delta H^0}{RT}, \quad (4)$$

where R (8.314 J mol^{-1} K^{-1}) is the universal gas constant, $K_T = q_e/C_e$ is the distribution coefficient, ΔH (kJ mol^{-1}) is the enthalpy change, T (K) is the absolute temperature, ΔG (kJ mol^{-1}) is the free energy change, and ΔS (J mol^{-1} K^{-1}) is the entropy change.

2.7. Reusability of MS-AC materials

A series of successive reusability tests were performed to explore the recovery and efficiency of utilized MS-AC adsorbents for the removal of MB. For the desorption experiment, three solvents, including 0.1 M HCl, 95% ethanol, and 0.1 M NaOH, were evaluated. First, 50 mL of 100 mg L^{-1} MB and 75 mg of MS-AC were thoroughly mixed in an Erlenmeyer flask. The resulting mixture was heated at 298 K and 120 rpm for 40 min. The MS-AC/MB solid was then recovered by centrifugation, washing with DI water, and drying at 343 K in an oven. The dry MS-AC/MB was then subsequently soaked in 20 mL of ethanol and stirred for 40 min at 120 rpm. After stirring, the MS-AC material was separated and dried at 333 K for two hours before use in the subsequent adsorption cycle to eliminate MB. Each experiment was conducted in triplicate.

2.8. Concentrations of MB in real and simulated wastewater samples

The concentration of MB in synthetic and wastewater samples was quantified using a UV-vis spectrophotometer (UV-2900, Hitachi, Japan) at 665 nm. A six-point calibration curve was first constructed using a standard concentration of MB (5, 30, 55, 80, 105, and 130 mg L^{-1}) before quantifying the amount of MB in wastewater samples. To evaluate the selectivity of the as-prepared adsorbent, a simulated wastewater solution consisting of 100 mg L^{-1} each of rhodamine B, methylene blue, methylene orange, and Procion brilliant blue was prepared. The adsorption experiment was conducted by adding 300 mg of MS-AC to 100 mL of simulated wastewater at pH 8, a temperature of 298 K, and a contact time of 2.4 hours. The concentration of each dye was then determined using a UV-vis spectrophotometer at the following wavelengths: 450 nm for MO, 554 nm for Rh6B, 665 nm for MB, and 594 nm for PBB.

3. Results and discussion

3.1. Bulk and surface characterizations

The crystalline behavior, elemental composition, and functional groups of the as-prepared raw *Maerua subcordata* (RMS) tuber powder and its activated carbon with sodium carbonate (MS-AC) were examined using XRD, FTIR spectroscopy, and XPS techniques. Fig. 1a presents the XRD results of both the RMS and MS-AC samples. The XRD result of the RMS sample displays a broad peak at $2\theta = 24.5°$ along with three distinct peaks at $2\theta = 21.3°$, $29.5°$, and $35.4°$. The diffraction peak at $2\theta = 21.3°$ corresponds to the (200) plane of cellulose I, the naturally occurring crystalline form of cellulose in plant biomass, while
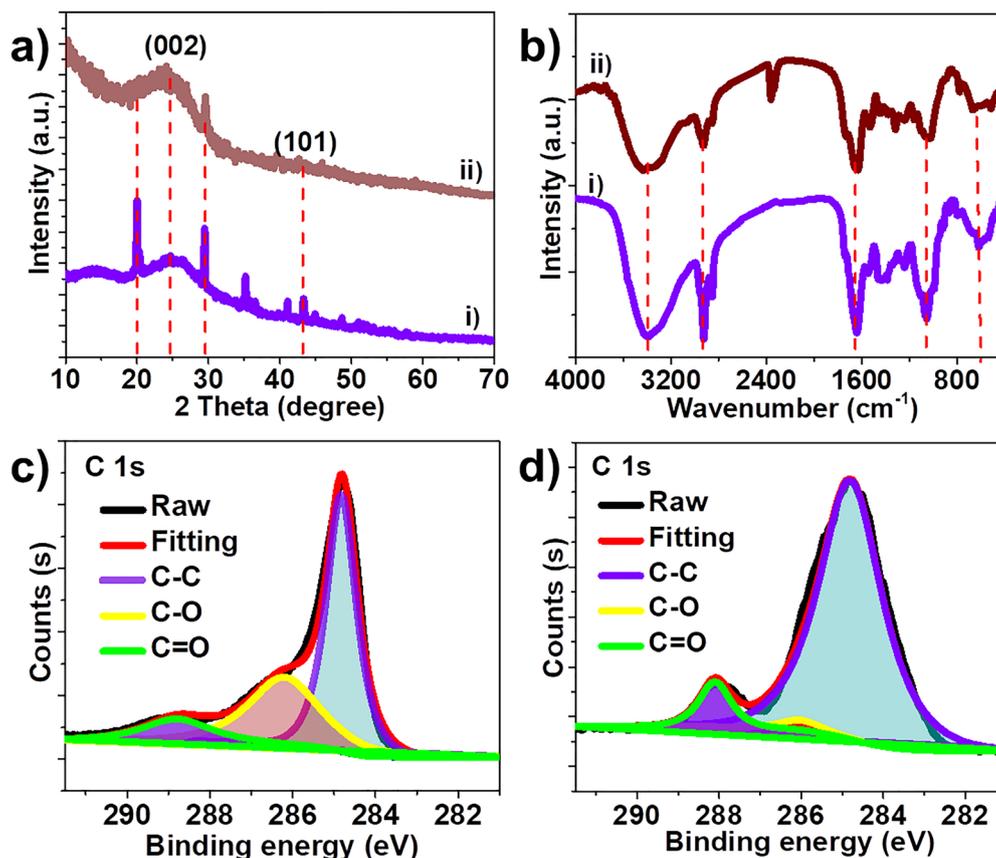
Fig. 1 XRD patterns (a) and FTIR spectra (b) of the as-prepared MS raw carbon sample (i) and the activated MS carbon sample (ii). C 1s XPS spectra of the (c) as-prepared MS raw carbon sample and (d) activated MS carbon sample.

the peaks at $2\theta = 29.5°$ and $35.4°$ are attributed to crystalline impurities, specifically calcite ($CaCO_3$), a common inorganic ash component in plant-derived materials.[33] In contrast, the MS activated with sodium carbonate (MS-AC) does not exhibit these sharp peaks but instead shows broad peaks at $2\theta = 24.6°$ and a highly diminished peak at 2θ of $43.2°$, indicating that the MS-AC sample has a higher degree of amorphousness than that of the RMS sample. These features are typical of the chaotic, amorphous graphite-like carbon structure, which is crucial for the adsorption of pollutants from environmental samples due to its inherently porous nature.[31] The relative crystalline size, calculated employing the Scherrer formula based on the broad peak at $2\theta = 24.6°$, was found to be less than 3 nm. This suggests a microporous property of the as-prepared material. We employed FTIR spectroscopy measurements to scrutinize the characteristic groups in both RMS and activated MS-AC samples. Fig. 1b shows the FTIR spectra of RMS and MS-AC, acquired from frequencies of 4000 to 400 cm^{-1}. The FTIR result of the RMS sample revealed a wide peak at 3395 cm^{-1}, which matches the stretching frequency of O–H. The peak at 2936 cm^{-1} is associated with the stretching vibrations of C–H bonds in aliphatic hydrocarbons.[34] A characteristic peak centered at 1651 cm^{-1} in the RMS sample is ascribed to the carbonyl stretching of carboxylic acids, ketones, and aldehydes.[30] The characteristic absorption band at 1551 cm^{-1} is assigned to the

$C{=}C$ stretching vibration within the aromatic ring system.[35] Additionally, the peaks at 1051 cm^{-1} and 625 cm^{-1} in the RMS sample correspond to the stretching of C–O and the out-of-plane bending of aromatic C–H, respectively.[36] The FTIR spectra of the activated MS (MS-AC) are also presented in Fig. 1b. The O–H stretching peaks for MS-AC are slightly broader and appear at a higher frequency (3398 cm^{-1}) than those of the raw MS. A closer inspection at the MS-AC spectra shows minor shifts in the C–H, C–O, and $C{=}O$ stretching to 2936 cm^{-1}, 1053 cm^{-1}, and 1657 cm^{-1}, respectively, indicating a structural change after chemical activation. Besides, the intensity of most of the FTIR peaks for MS-AC is significantly reduced, suggesting the removal of functional groups present in volatile components.[37] Interestingly, the activated MS (MS-AC) sample exhibits a new peak at 2365 cm^{-1}, which primarily corresponds to adsorbed CO_2. This peak is commonly seen in the FTIR spectra of porous materials such as activated carbons.[38]

To gain deeper insights, we also analyzed the C 1s XPS spectra both before and after the activation of the MS samples. The survey spectra in Fig. S1 show the presence of carbon and oxygen in both RMS and MS-AC samples. Fig. 1c and d display the high-resolution XPS spectra of C 1s of RMS and MS-AC, respectively. As displayed in Fig. 1c, the C 1s XPS spectra of the RMS sample were fitted to three main peaks placed at 288.1, 286.0, and 284.8 eV, corresponding to carbonyl groups ($C{=}O$),

ether groups (C–O), and graphitic carbon (C–C), respectively. The C 1s XPS spectra of the MS-AC sample displayed similar oxygen-containing functional groups but with slightly lower peak intensities than those of the RMS sample (Fig. 1d). Quantitative analysis based on the XPS peak area ratios (Fig. 1c and d) shows that the carbon content after activation increased from 38% to 57%. This indicates a reduction in oxygen-containing functional groups following activation with Na_2CO_3 and carbonization.

3.2. Morphological and surface area studies

We utilized SEM and SEM/EDX to further investigate the elemental composition and morphological features of the samples before and after activation. The SEM image of the activated MS sample (MS-AC) is shown in Fig. 2a. As illustrated, the MS-AC sample exhibits a porous architecture, characterized by interwoven and interconnected oval-shaped structures with relatively uniform dimensions. In contrast, the non-activated sample (RMS) displays a more compact and flattened morphology with minimal pore development (Fig. S2a), highlighting the significant structural changes induced by the activation process. To further assess the elemental composition and spatial distribution, we performed SEM/EDX elemental mapping on both

RMS and MS-AC samples. As shown in Fig. 2b, the MS-AC sample has a higher carbon content compared to the RMS sample (Fig. S2b), suggesting an increased degree of graphitization after activation that is similar to the XPS results. Additionally, the SEM/EDX elemental maps of MS-AC (Fig. 2c–e) reveal an even distribution of carbon and oxygen all over the structure. In contrast, the RMS sample exhibits a noticeably non-uniform elemental distribution (Fig. S2c–e), further demonstrating the effect of activation on structural homogeneity. The nitrogen physisorption isotherms were conducted to examine the surface area and pore size distribution of the raw MS and activated MS adsorbents. Fig. 2f shows the N_2 physisorption isotherms for the RMS and MS-AC samples prepared in this study. The determined BET surface areas for the RMS and MS-AC were 113 m^2 g^{-1} and 370 m^2 g^{-1}, respectively. The higher surface areas of the activated MS sample may be attributed to the presence of more porous moieties in its structure, which is consistent with the findings from the SEM images. The isotherms for both samples can be categorized as type II and type IV behaviors, suggesting the existence of mesopores and macropores within the as-prepared materials. As shown in Fig. 2g, the BJH pore size distribution of both samples is broad, with a main peak centered at 48.4 nm. The activated MS exhibits a higher pore volume (0.162 cm^3 g^{-1})
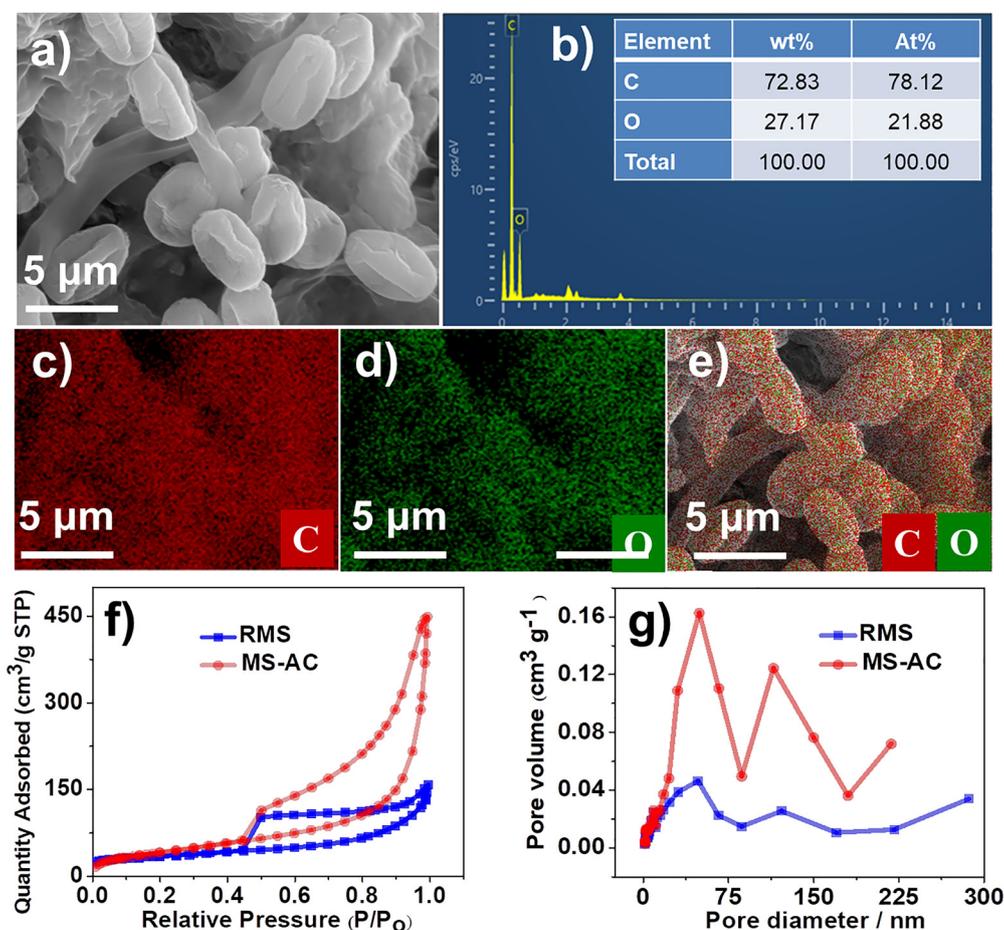

Fig. 2 SEM image (a), EDX spectra (b), corresponding EDX elemental mapping images (c) and (d), and overlay image (e) of the as-prepared activated MS sample. (f) Nitrogen physisorption isotherms and (g) BJH pore size distribution plot of the raw MS (RMS) and activated MS (MS-AC).

than that of the raw MS sample (0.0459 cm^3 g^{-1}), further demonstrating the presence of larger mesopores and macropores in the MS-AC structure.

3.3. Batch experiments

3.3.1. Activation effect. The adsorbent material derived from *Maerua subcordata* tuber powder was prepared both before and after activation, and its effectiveness in removing methylene blue from water samples was evaluated. Before conducting the adsorptive experiments, we established a six-point calibration curve using standard solutions of MB. The R^2 value of the calibration curve was 0.999 (Fig. S3a), confirming both the optimal linear fit and the correctness of the proposed method. The MB adsorption performance of the MS material was evaluated both before and after activation under consistent conditions: a contact time of 40 minutes, a concentration of 100 mg L^{-1} MB, 75 mg of adsorbent, a temperature of 298 K, and a stirring speed of 120 rpm. The activated MS material (MS-AC) achieved a maximum removal of 99.1%, while the non-activated MS material reached only 62.5% (Fig. S3b). The improved adsorption of MB by the MS-AC material is attributed to its amorphous structure and high porosity.

3.3.2. Surface charge density and effect of pH. To investigate the surface charge density of the activated MS material, we conducted a zeta potential measurement as a function of pH to examine the point of zero charge (pH$_{PZC}$). As presented in Fig. 3a, the pH$_{PZC}$ value of the MS-AC material was found to be 6.4. This indicates that at a pH of 6.4, the surface charge density of the material is zero, resulting from an equal number of negatively and positively charged sites. At a pH greater than

the pH$_{PZC}$, the surface of the MS-AC sample carries a negative charge, augmenting the uptake of cationic MB due to increased electrostatic attraction. Conversely, at a pH lower than the pH$_{PZC}$, the MS-AC surface has a net positive charge from H$^+$ ions, resulting in competition with MB and a reduction in dye adsorption.[39] The pH of the solution significantly influences the adsorption rate by altering the surface charge of the MS-AC sample. To evaluate this effect, we examined the adsorption of MB onto MS-AC across a pH range of 2 to 12, as shown in Fig. 3b. A lower removal percentage was observed at pH values below 6. This decrease is likely due to the elevated concentration of H$^+$ ions on the MS-AC surface under acidic conditions, which inhibits the adsorption of MB, which is cationic in nature. However, at higher pH levels, the increased abundance of negatively charged sites enhances the adsorption of the cationic dye. Therefore, at pH values higher than the pH$_{PZC}$, the negatively charged MS-AC surface favors the binding of positively charged MB molecules. The finding is consistent with the MB removal using *Buxus sempervirens* (Boxwood) leaf powder.[40]

3.3.3. Adsorbent dose. To inspect the influence of adsorbent dose, a set of tests were performed by changing the dosage from 15 mg to 115 mg (0.3 g L^{-1} to 2.3 g L^{-1}) while keeping the other conditions constant: contact time = 40 minutes, initial MB concentration = 100 mg L^{-1}, stirring speed = 120 rpm, temperature = 298 K, and pH = 8. As the dose increases from 15 mg to 75 mg, the removal efficiency of MB significantly rises, peaking at 99.4% at 75 mg (Fig. 3c). This enhancement is caused by the rise in active sites delivered by a larger quantity of adsorbent. However, as the dose increases beyond 75 mg,
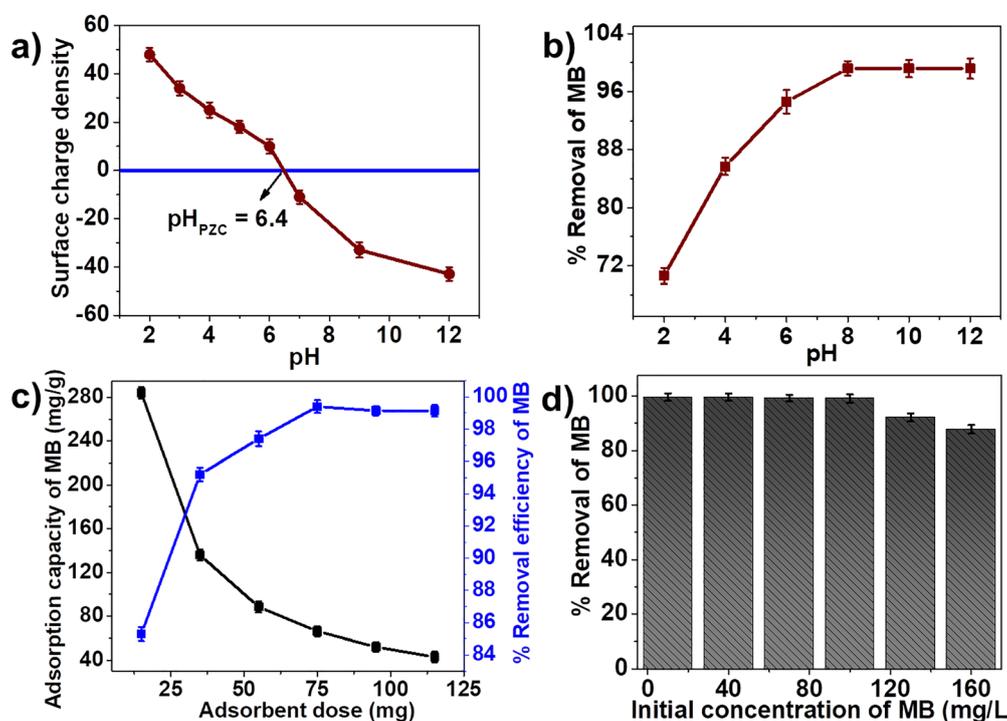

Fig. 3 Effect of the (a) pH$_{PZC}$, (b) pH, (c) adsorbent dose, and (d) initial concentration on the removal of MB using MS.

there is no significant change in removal efficiency, likely owing to the overlap of effective adsorption sites and the aggregation of adsorbent particles.[41] Therefore, a dose of 75 mg was deemed optimal. This finding agrees with previously reported research.[34]

3.3.4. Methylene blue concentration. The MB initial concentration effect on the adsorption efficiency of MS-AC was assessed by varying its value from 10 to 160 mg L^{-1} while keeping the dosage, pH, stirring speed, and temperature constant at 75 mg, 8, 120 rpm, and 298 K, respectively. As displayed in Fig. 3d, the removal percentage of MB dye slightly decreases as the concentration rises from 10 mg L^{-1} to 100 mg L^{-1}. However, when the concentration exceeds 100 mg L^{-1}, the percentage of MB removal decreases significantly, likely due to the reduced availability of adsorption sites with the increase in the concentration of MB dye. Thus, a concentration of 100 mg L^{-1} MB was chosen as the optimal value. The finding is consistent with the results obtained using other adsorbents.[42]

3.3.5. Contact time. The influence of time on the percentage removal of MB using MS-AC was studied by changing its value from 10 to 60 minutes while maintaining all other conditions the same: a dosage of 75 mg, a pH of 8, a stirring speed of 120 rpm, and a temperature of 298 K. As shown in Fig. 4a, the adsorption efficiency quickly increases as the contact time extends from 10 to 30 minutes, indicating the availability of numerous active sites on the MS-AC material. The adsorption system then reached equilibrium within the next 40 minutes, at which point the MB removal efficiency remained stable, suggesting that the active sites on MS-AC may be fully occupied by dye molecules.[43] At 40 minutes, the highest MB removal efficiency was determined to be 99.2%. Beyond this

time, a steady state in the adsorption process was observed, indicating that additional contact time does not increase the percentage removal of the dye. Therefore, a contact time of 40 minutes was identified as the optimal value. These results are consistent with the results reported in the literature, which were obtained using a carboxymethyl cellulose-based silica hydrogel nanocomposite as an adsorbent.[44]

3.3.6. Mixing speed. The influence of mixing speed on the removal of MB was investigated by fluctuating the agitation rate from 40 to 200 rpm while keeping all other experimental variables constant. At lower agitation rates, limited fluid motion restricted the movement of MB from the bulk solution to the adsorbent surface, resulting in lower removal efficiency. As the agitation speed increased, enhanced turbulence reduced the thickness of the boundary layer near the adsorbent, promoting faster mass transfer and improving dye uptake. Maximum adsorption performance was achieved at an agitation speed of 120 rpm, indicating sufficient contact between the MB dye and the available active sites on MS-AC.[1] Beyond this speed, insignificant enhancement in adsorption efficiency was perceived, suggesting that the adsorption sites had reached saturation and that additional mechanical energy no longer contributed to further dye capture. Therefore, 120 rpm was identified as the most effective agitation speed in this study.

3.3.7. Effect of salinity and competing dyes. To evaluate the effect of salinity, we assessed the efficiency of the as-prepared material in the presence of different concentrations of inorganic salts including NaCl, MgCl$_2$, CaCl$_2$, and AlCl$_3$ (Fig. 4c). The MB removal efficiency decreased with the increase in the ionic concentration of each salt, possibly because competition between the cationic MB and the hydrated cations for
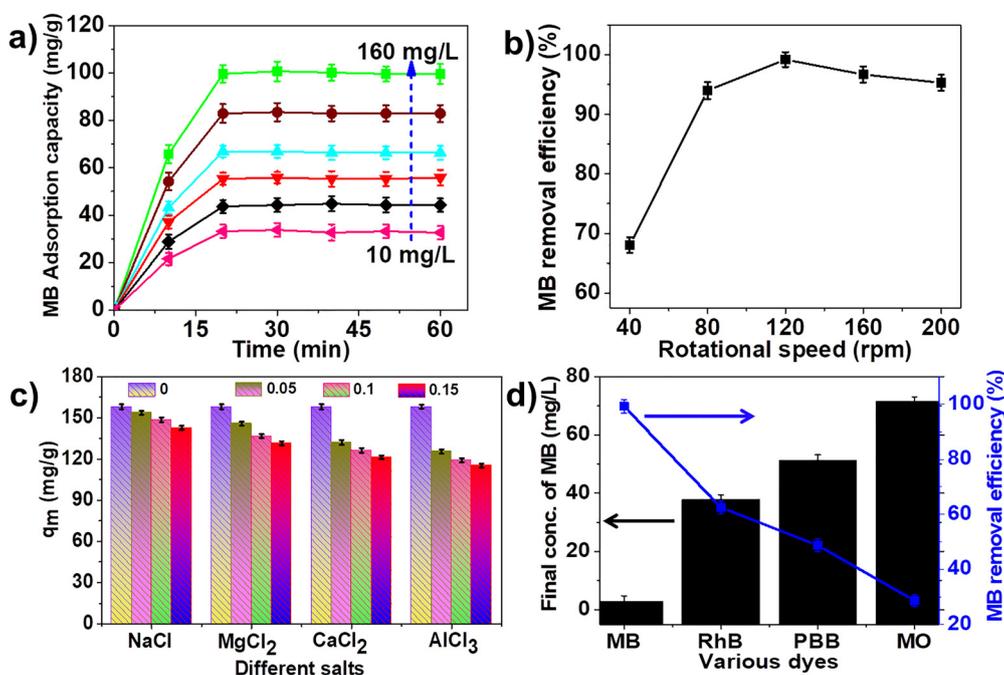

Fig. 4 Effect of the (a) time, (b) rotational mixing speed, (c) coexisting cations, and (d) coexisting dyes on the removal of MB from MS-AC.

active sites on MS-AC limits the movement of MB to the surface of the MS-AC sample.[30] In other words, the increase in the ionic strength of the salt weakens the electrostatic interaction between the adsorbent and the adsorbate, while the hydrophobic interactions increase because the increase in the viscosity of the solution (resulting from the salt concentration) diminishes the conveyance of the MB ions to the adsorbent surface.[14] This suggests that hydrophobic interactions are the primary causing factor in this process, which occurred under high-salt conditions. The MB removal efficiency in the presence of different salts followed the pattern of $NaCl > MgCl_2 > CaCl_2 > AlCl_3$. We also assessed the adsorption efficiency of MS-AC in simulated wastewater containing rhodamine B (RhB), methylene blue (MB), methylene orange (MO), and Procion brilliant blue (PBB). The adsorptive removal of RhB, MB, MO, and PBB on MS-AC was found to be 62.5%, 99.2%, 28.6%, and 48.7%, respectively (Fig. 4d). The results demonstrated that MS-AC selectively adsorbed MB over the other dyes in the simulated wastewater solution, with the adsorption efficiency following the order of MB > RhB > PBB > MO. The higher adsorption efficiency of MB compared to the other dyes can be attributed to its stronger electrostatic interactions, enhanced π–π interactions, smaller molecular size, and improved pore accessibility relative to the other tested dyes. At the working pH (> 8), the MS-AC surface carries a negative charge, promoting strong electrostatic attraction with the cationic MB. In contrast, the anionic dyes MO and PBB face electrostatic repulsion, resulting in significantly lower uptake.[45,46] Furthermore, although

rhodamine B (RhB) is cationic, methylene blue demonstrates higher adsorption because of its smaller molecular size and more planar aromatic structure, which facilitates easier diffusion into the micro- and meso-porous structure of MS-AC.[47,48] This also enables stronger π–π stacking interactions with the graphitic domains of the MS-AC sample. The planar thiazine ring system of MB enhances overlap with the conjugated carbon surface, strengthening adsorption compared to the bulkier, less planar RhB molecule. These combined effects account for the partial selectivity of MS-AC for MB. We also compared the order of methylene blue selectivity in the presence of various cationic and anionic dyes with the state of the art. As shown in Table S1, our findings are consistent with the results previously published in the literature.

3.4. Adsorption isotherm

To examine the adsorption behavior of MB on MS-AC, we conducted adsorption isotherm studies using various concentrations of MB ranging from 10 to 160 mg L^{-1} at 25 °C, pH 8, a stirring speed of 120 rpm, an adsorbent dosage of 75 mg, and a contact time of 40 minutes. Four adsorption isotherms, namely Langmuir, Freundlich, Temkin, and Dubinin–Radushkevich, were employed to fit the data (Fig. 5). The mathematical equations, the meaning of the individual terms, and a summary of the relevant physical quantities for each isotherm model are provided in the SI. We employed the Langmuir and the Freundlich model to best explain the adsorption of adsorbates on a homogeneous adsorbent surface and heterogeneous
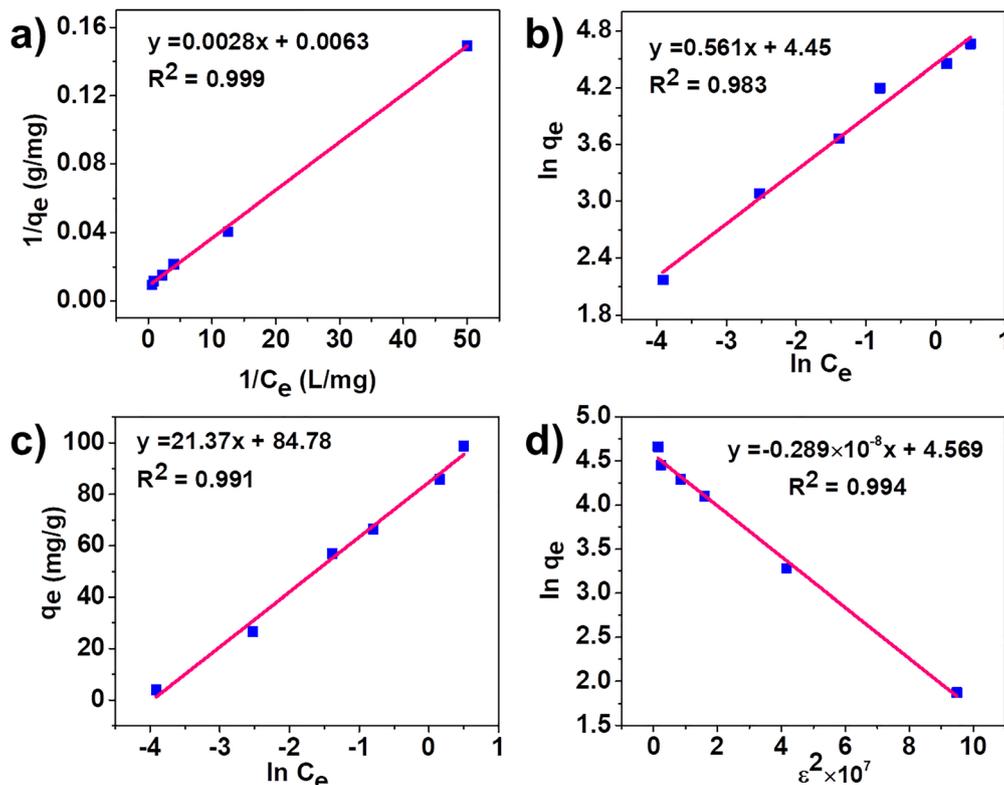

Fig. 5 (a) Langmuir, (b) Freundlich, (c) Temkin, and (d) Dubinin–Radushkevich linearized isotherm models for the adsorption of MB on MS-AC.

surfaces, respectively, while we used the Temkin and D–R model to more intriguingly differentiate the adsorption mechanism. The Langmuir model characterizes single-layer adsorption on a homogeneous surface, the Freundlich model describes adsorption on heterogeneous surfaces, and the D–R model offers a more comprehensive understanding of the adsorption mechanism. Fig. 5 shows different linearized isotherm models for MB adsorption onto MS-AC. As shown in Fig. 5 and Table S2, the R^2 values follow the order of Langmuir > D–R > Freundlich > Temkin. This indicates that the Langmuir model provides the best fit for our experimental data, with the highest linear R^2 value of 0.999. This suggests that the adsorption of MB onto MS-AC likely occurs *via* monolayer coverage on a homogeneous adsorbent surface. The maximum adsorption capacity and the Langmuir adsorption constants were 158.7 mg g^{-1} and 2.25 L mg^{-1}, respectively (Table S2). Additionally, we evaluated the dimensionless factor (R_L) to assess the feasibility of the reaction. The R_L values ranged from 0.003 to 0.04 for concentration levels between 10 and 160 mg L^{-1}, indicating that the adsorption of MB onto MS-AC was highly favorable. An R_L value greater than 1.0 indicates an unfavorable adsorption isotherm, while an R_L value equal to 1.0 indicates linear behavior, and an R_L value of 0 indicates irreversible adsorption.[49] The adsorption capacity value (n_f) determined from the Freundlich model was found to be approximately 2 (Table S2), indicating that it is within the acceptable range and that the adsorption process is effective.[50] According to the Temkin model, the binding energy constant (b) exhibited positive values (Table S2), suggesting that the adsorption process is endothermic

in nature.[51] From the D–R model, the calculated average adsorption energy was 13.1 kJ mol^{-1}, signifying that chemisorption is a primarily cause for the adsorption of MB onto MS-AC.

3.5. Adsorption kinetics

The kinetic studies of MB adsorption onto MS-AC were conducted using the pseudo-second-order (PSO), intraparticle diffusion (IPD), pseudo-first-order (PFO), and Boyd kinetic models (Fig. 6). The experiments varied the duration from 10 to 70 minutes while maintaining all variables constant: a 100 mg L^{-1} concentration of MB, pH 8, a mixing speed of 120 rpm, a dose of 75 mg, and a 298 K temperature. To calculate the parameters for each kinetic model, we used the slopes and intercepts from the corresponding graphs (Fig. 6 and Table S3). Among the four kinetic models employed, the PSO model delivered the highest R^2 value (0.999), indicating that the MB adsorption on MS-AC is best explained by this model. The adsorption of MB followed a PSO with a rate constant of 0.0066 g mg^{-1} min^{-1} for the 100 mg L^{-1} MB solution. Furthermore, the q_e value calculated from the PSO model (67.6 mg g^{-1}) meticulously aligns with the experimental q_e value (66.4 mg g^{-1}) (Table S3), suggesting that MB dye adsorption onto MS-AC may follow a chemisorption process. We further analyzed the data using the IPD model to assess the impacts of adsorbent size and surface area on the adsorption process. We employed the intraparticle diffusion model equation, detailed in Table S3, to evaluate the key kinetic parameters. As shown in Fig. 6c, the fitted curve does not pass through the origin and reveals two distinct regions:
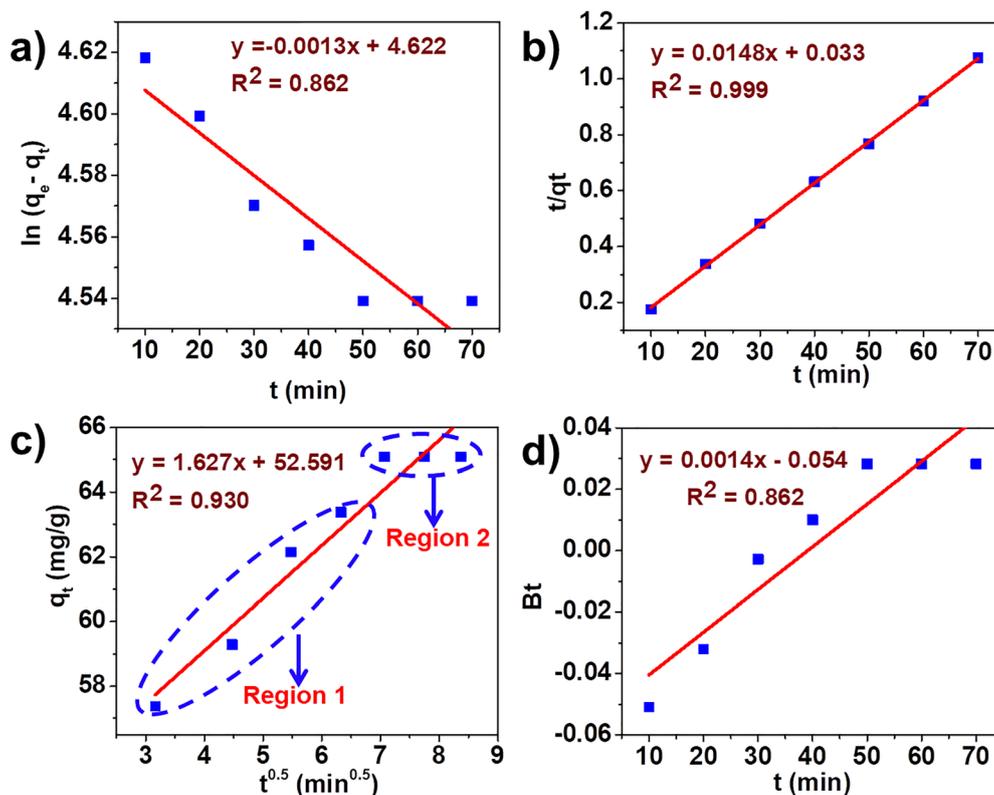

Fig. 6 Kinetic studies for the adsorption of MB on the MS-AC sample: (a) PFO, (b) PSO, (c) IPD, and (d) Boyd model plots.

the diffusion of MB through the solution or boundary layer to the outer surface of the MS-AC sample (region 1) and the diffusion of MB into the pores of the MS-AC sample (region 2).[30] The calculated C value, which is significantly different from zero (see Table S3), indicates that both intraparticle diffusion and mass transfer contribute to the adsorption rate of MB. Based on the IPD findings, it was difficult to determine which mode had a greater effect on MB adsorption onto the adsorbent. Thus, we further analyzed the experimental data using the Boyd kinetic model to identify the real rate-determining step of the adsorption of MB dye over MS-AC (Fig. 6d and Table S3). The lack of linearity passing through the origin indicates that the external mass transfer, specifically film diffusion, is the dominant rate-controlling step rather than intra-particle diffusion (Fig. 6d).[52]

3.6. Thermodynamic study

The effect of temperature was examined by adjusting its value from 25 °C to 40 °C. The temperature change showed a slight escalation in the removal percentage of MB when the temperature was changed from 298 K to 313 K (Fig. S4a). We employed the van't Hoff equation, plotting $\ln K_T$ against $1/T$, to evaluate the thermodynamic variables including standard entropy change ($\Delta S°$ from the intercept), free energy change (ΔG), and enthalpy change ($\Delta H°$ from the slope). Fig. S4b shows this plot of $\ln K_T$ versus $1/T$. The $\Delta G°$ values were negative (Table S4), demonstrating that the adsorption of MB onto MS-AC is feasible and spontaneous. However, the $\Delta H°$ value was obtained to be positive (+106.4 kJ mol^{-1}), demonstrating that the adsorption is endothermic. Based on the $\Delta H°$ value, which lies between 40 and 120 kJ mol^{-1}, the chemisorption process plays a great role in the adsorption mechanism.[1] This is also corroborated by XPS and FTIR analyses presented in the upcoming section. Moreover, the $\Delta S°$ value (+398.8 J mol^{-1} K^{-1}) indicates increased disorder at the solid–liquid interface, which enhances adsorption.

3.7. Regeneration experiments

To evaluate the reusability of the as-prepared adsorbent, we conducted a series of adsorption–desorption experiments employing three solvents, namely, HCl, ethanol, and NaOH (Fig. S5). As shown in Fig. S5, ethanol was the most effective solvent for desorbing MB from the MS-AC sample. After four cycles of reusability test, the MB removal efficiency was found to be 92.7%, 84.3%, and 71.4% using ethanol, HCl, and NaOH, respectively. This implies that over 90% of the original removal efficiency (99.2%) was maintained after four cycles of adsorption–desorption when using ethanol. Thus, MS-AC can be employed as an economically efficient and reusable material for treating wastewater containing MB. The findings in the present study are consistent with the previously reported results.[53]

3.8. Real sample analysis and comparison with the literature

The practical capability of the MS-AC adsorbent was also investigated by assessing its ability to remove MB from real wastewater samples collected from industries. Under optimal conditions outlined in this study, the MS-AC sample reduced the concentration of MB dye in the wastewater sample (0.12 mg L^{-1}) to 0.004 mg L^{-1}. This result indicates that the removal efficiency of MB by the as-prepared MS-AC adsorbent was 96.7% in wastewater samples, demonstrating the practical capability of this adsorbent in real-world applications. The adsorption performance of MS-AC in removing MB was compared to that of various bio-adsorbents. MS-AC exhibited the highest MB dye removal efficiency compared with many adsorbents listed in Table 1, indicating that MS-AC is a highly effective option for eliminating MB from aqueous environments.

3.9. Adsorption mechanism

The surface charge density and pH-dependent studies discussed in the previous section confirm the presence of electrostatic

Table 1 Assessment of the maximum adsorption capacity of MS-AC for methylene blue compared with state-of-the-art adsorbents

No	Adsorbent	q_m (mg g^{-1})	Adsorbent dose (g L^{-1})	MB concentration range (mg L^{-1})	Temperature (°C)	pH	Time (min)	Isotherm	Kinetics	Ref.
1	Potato peel	25.0	8	10–50	25	6.5	60	Langmuir	PSO	39
2	Pine tree leaves	126.6	1.0	10–90	30	9.2	240	Langmuir	PSO	54
3	Gulmohar leaf powder (GUL)	186.2	1	50–200	30	7	1440	Langmuir	PSO	55
4	Lotus leaf	221.7	1	1–5	20	7	120	Koble–Corrigan	PSO	56
5	Oak sawdust (hydrolyzed)	38.5	4	2–10	25	7	180	Freundlich	PSO	57
6	Eucalyptus leaves (raw)	66.0	0.15	1–5	25	10	120	N/A	PSO	58
7	Co-doped Fe-BDC MOF	23.9	1	1–7	50	4	70	Langmuir	PSO	59
8	Chitosan/fly ash	263.2	0.9	7.7–59.7	(N/A)	4	50	Freundlich	PSO	60
9	*Ziziphus spina-christi* seed (ZSCS)	666.7	0.6	50–500	45	6	30	Langmuir	PSO	61
10	P$_2$Mo$_{18}$/MIL-101(Cr)	312.5	0.6	50–200	25	6	30	Langmuir	PSO	62
11	*Juncus effusus* (raw)	1.421	1.5	10–50	(N/A)	7	120	Freundlich	PSO	63
12	Eucalyptus wood (modified)	380.4	0.03	100	25	9	720	Langmuir	PSO	64
13	Coal fly ash-activated	323.6	2	2–10	25	10	60	Langmuir	PSO	65
14	Barley bran (BB)	63.2	2.5	10–165	25	5.07	240	Langmuir	PSO	66
15	Enset midrib leaf	35.5	2.5	10–105	25	5.66	120	Langmuir	PSO	66
16	Bulrush plant (activated)	41.2	20	25–100	26	8	60	Langmuir	PSO	67
17	Lupine seed (Lu-SP)	77.5	0.2	10–100	25	8	120	Langmuir	PFO	68
18	Rice straw	40.6	3.0	20–100	30	7	120	Langmuir	PSO	69
19	*Maerua subcordata* tuber (activated)	158.7	1.5	10–160	25	8	40	Langmuir	PSO	This study

interactions, implying their importance in the adsorption mechanism. Furthermore, MB can be adsorbed onto the MS-AC sample through π–π stacking interactions because both MB and MS-AC contain aromatic rings, which further contribute significantly to the adsorption process (Scheme S1). To improve the understanding of the adsorption mechanism, we performed FTIR spectroscopy and XPS measurements on MS-AC both before and after the adsorption of MB (Fig. 7). Fig. 7a reveals the FTIR spectra of MS-AC before and after the MB adsorption. The O–H stretching peaks for MS-AC, centered at 3398 cm^{-1}, shifted to 3401 cm^{-1} after adsorption, suggesting the construction of hydrogen bonding between MS-AC and MB. Furthermore, the peaks centered at 1657 cm^{-1} and 1053 cm^{-1}, corresponding to the symmetric stretching of C=O and C–O, respectively, shifted to 1662 cm^{-1} and 1057 cm^{-1} for the MS-AC/MB solid. These shifts, together with a reduction in the intensity of the FTIR peaks, show that these functional groups play a significant role in the adsorption process. We employed XPS techniques to further examine the surface interaction between MB and MS-AC. Fig. 7b shows the survey spectra of MS-AC before and after the adsorption of MB. As shown in Fig. 7b, the survey spectrum of MS-AC before the adsorption of MB mainly shows the presence of C and O. However, the survey spectrum of MS-AC after the adsorption of MB revealed the presence of the

S 2p peak at 164.5 eV and the Cl 2p peak at 198.9 eV, in addition to the O 1s and C 1s signals. The presence of S and Cl, constituent elements of MB, indicates the successful MB adsorption over the MS-AC surface.[34] To gain further insights into the adsorption mechanism, we analyzed the high-resolution O 1s and C 1s spectra of MS-AC before and after MB adsorption (Fig. 7c and d). The C 1s spectrum of MS-AC recorded before MB adsorption was deconvoluted into three distinct peaks centered at 288.0, 286.0, and 284.4 eV, corresponding to O–C=O, C–O/C=O, and graphitic carbon functional groups, respectively. After the adsorption of MB onto MS-AC, the binding energy of these peaks slightly shifted to 288.1, 286.3, and 284.85 eV. This shift indicates the transfer of an electron from the MS-AC sample to the MB molecule, further corroborating strong interactions between MB and the MS-AC functional groups. The O 1s spectrum of MS-AC before the adsorption of MB was also deconvoluted into three peaks, centered at 529.9, 531.3, and 532.2 eV, attributed to oxygen in carbonyl groups, hydroxyl/ether groups, and surface-adsorbed oxygen or water molecules, respectively (Fig. 7d). After MB adsorption, these peaks were slightly shifted to higher binding energies, indicating the electron density redistribution around oxygen atoms, confirming their participation in surface chemical interactions with MB molecules.[30]
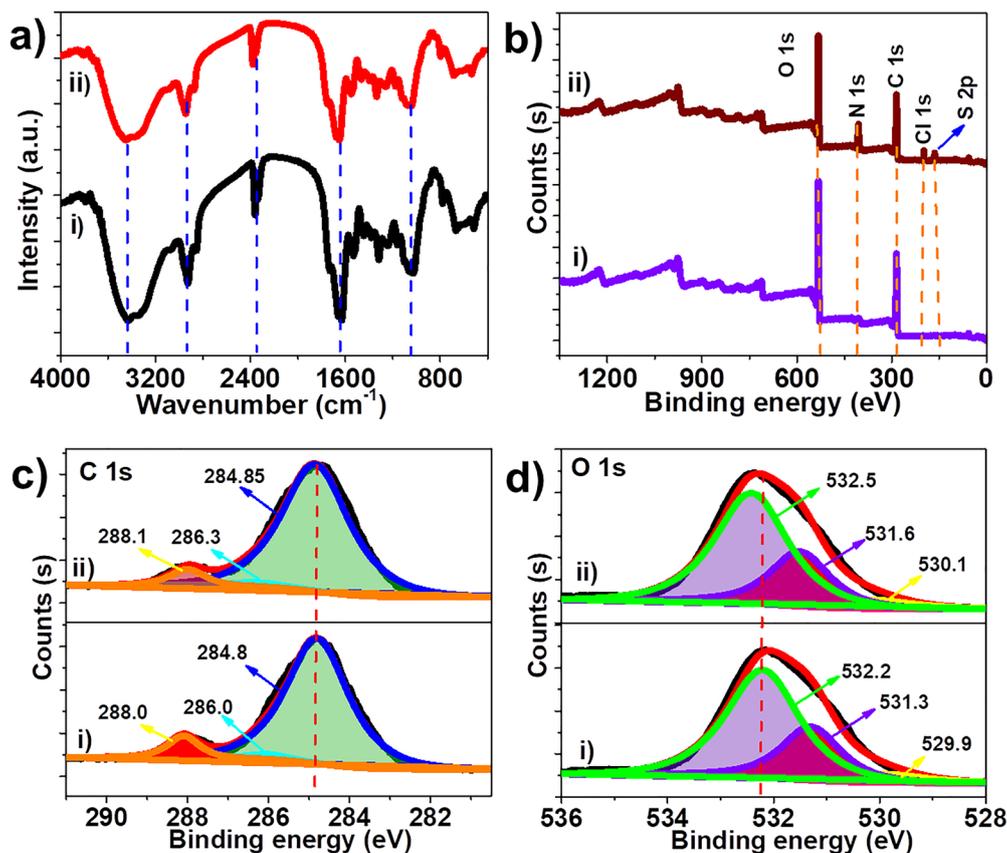

Fig. 7 (a) FTIR spectra, (b) survey XPS spectra, (c) C 1s, and (d) O 1s XPS spectra of MS-AC before and after the adsorption of MB. Here, (i) refers to the spectra before adsorption while (ii) refers to the spectra after adsorption.

4. Conclusion

Herein, a low-cost and sustainable AC derived from *Maerua subcordata* tubers was successfully synthesized *via* Na_2CO_3 activation followed by thermal treatment. Physicochemical characterization using XRD, XPS, SEM, and FTIR spectroscopy confirmed the formation of a highly amorphous, porous structure enriched with surface functional groups, which played a critical role in enhancing the adsorption performance. The as-prepared MS-AC sample exhibited excellent adsorption capability toward MB, achieving a high adsorption capacity of 158.7 mg g^{-1} at 25 °C, which is superior to many previously reported adsorbents. The adsorption was well explained by the Langmuir model, demonstrating single-layer adsorption on a relatively homogeneous surface. The PSO kinetic model was the best to describe the adsorption process. The thermodynamic studies revealed that ΔG° was found to be negative, while the ΔH° value was positive (ΔH° = +106.4 kJ mol^{-1}), indicating that the adsorption process was spontaneous, endothermic, and chemisorptive in nature, respectively. The MS-AC sample displayed excellent selectivity toward MB in mixed-dye systems and remarkable reusability, maintaining over 90% of its original removal efficiency after four adsorption–desorption cycles using ethanol as the regenerating agent. Moreover, when applied to real wastewater samples, the adsorbent achieved a high MB removal efficiency of 96.7%, demonstrating its practical applicability. Overall, the results underscore the potential of abundantly available biomass-derived activated carbons as efficient, selective, and economically viable adsorbents for the removal of organic pollutants from wastewater systems.

Conflicts of interest

The authors declare that they have no known conflicts of interest.

Data availability

The data that support the findings of this study are available from the corresponding author upon reasonable request. All relevant data used in the analysis have been included in the article and its supplementary information (SI). Supplementary information is available. See DOI: https://doi.org/10.1039/d6ma00030d.

Acknowledgements

References

1   B. T. Belayneh, B. Getahun, T. A. Berhe, B. A. Aragaw, Z. G. Workneh and A. A. Dubale, *Mater. Adv.*, 2025, **6**, 8574–8585.

2   M. Yousefi, S. Fallahizadeh, Y. Maleki, A. Sheikhmohammadi and A. Rezagholizade-Shirvan, *Sci. Rep.*, 2025, **15**, 20705.

3   D. N. Shetty, V. A. Lobo, S. Rani and N. Raghavendra, *Hybrid Adv.*, 2024, **7**, 100316.

4   A. Das, *Discover Civ. Eng.*, 2025, **2**, 139.

5   J. Lagiewka, K. Witt, M. Gierszewska and I. Zawierucha, *J. Water Process Eng.*, 2024, **68**, 106306.

6   Z. S. Tahseen, B. Z. Rashid, S. H. Ali, K. N. Kaka and S. J. Salih, *J. Hazard. Mater. Adv.*, 2025, **18**, 100686.

7   P. O. Oladoye, M. Kadhom, I. Khan, K. H. H. Aziz and Y. A. Alli, *Green Chem. Eng.*, 2024, **5**, 440–460.

8   M. N. Abonyi, C. C. Obi and J. T. Nwabanne, *Next Mater.*, 2025, **8**, 100696.

9   L. Zeghoud, M. Gouamid, O. B. Mya, A. Rebiai and M. Saidi, *Water, Air, Soil Pollut.*, 2019, **230**, 195.

10 R. S. P. Mak and E. L. Liebelt, *Pediatr. Emerg. Care*, 2021, **37**, 474–477.

11 F. Younas, A. Mustafa, Z. U. R. Farooqi, X. Wang, S. Younas, W. Mohy-Ud-Din, M. A. Hameed, M. M. Abrar, A. A. Maitlo, S. Noreen and M. M. Hussain, *Water*, 2021, **13**, 215.

12 A. S. Elsherbiny, A. Rady, R. M. Abdelhameed and A. H. Gemeay, *Environ. Sci. Pollut. Res. Int.*, 2023, **30**, 106860–106875.

13 N. Khatoon, N. Ali, H. Yang and W. Jun, *Desalin. Water Treat.*, 2024, **317**, 100092.

14 Y. Li, C. Gao, J. Jiao, J. Cui, Z. Li and Q. Song, *ACS Omega*, 2021, **6**, 33961–33968.

15 S. Naghdi, M. M. Shahrestani, M. Zendehbad, H. Djahaniani, H. Kazemian and D. Eder, *J. Hazard. Mater.*, 2023, **442**, 130127.

16 T. Takele, K. Angassa, M. Abewaa, A. M. Kebede and I. Tessema, *Biomass Convers. Biorefin.*, 2023, **15**, 4085–4108.

17 G. Ö. Kayan and A. Kayan, *J. Inorg. Organomet. Polym. Mater.*, 2022, **32**, 2781–2792.

18 I. Salahshoori, Q. Wang, M. A. L. Nobre, A. H. Mohammadi, E. A. Dawi and H. A. Khonakdar, *Adv. Colloid Interface Sci.*, 2024, **333**, 103281.

19 P. Nuengmatcha, A. Kuyyogsuy, P. Porrawatkul, R. Pimsen, S. Chanthai and P. Nuengmatcha, *Water Sci. Eng.*, 2023, **16**, 243–251.

20 A. Akinyemi, O. Agboola, E. Alagbe and E. Igbokwe, *Desalin. Water Treat.*, 2024, **320**, 100780.

21 A. S. Hasan, S. K. Dutta, A. Bashar, P. K. Dhar and R. Haque, *Sustainability Circ. NOW*, 2025, a26302599, DOI: 10.1055/a-2630-2599.

22 S. S. A. Kumar, S. Bashir, M. Pershaanaa, F. Kamarulazam, N. M. Saidi, Z. L. Goh, I. A. W. Ma, V. Kunjunee, A. Jamaluddin, K. Ramesh, S. Ramesh, S. Ramesh and R. Manikam, *J. Mater. Sci.*, 2023, **58**, 6516–6555.

23 W. M. Alghamdi and I. El Mannoubi, *Processes*, 2021, **9**, 1279.

24 A. H. Hashem, E. Saied and M. S. Hasanin, *Sustainable Chem. Pharm.*, 2020, **18**, 100333.

25 I. Shahzadi, S. Mubarak, A. Farooq and N. Hussain, *Aqua Water Infrastruct. Ecosyst. Soc.*, 2023, **72**, 914–929.

26 M. Abewaa, A. Mengistu, T. Takele, J. Fito and T. Nkambule, *Sci. Rep.*, 2023, **13**, 14701.

27 M. Megersa, A. Beyene, A. Ambelu and L. Triest, *Desalin. Water Treat.*, 2017, **59**, 127–134.

28 W. R. Kangor, K. Ayabei, S. Lutta and G. Maiyoh, *J. Agric. Chem. Environ.*, 2021, **10**, 305–313.

29 H. N. Hamad and S. Idrus, *Polymers*, 2022, **14**, 783.

30 S. Sahu, S. Pahi, S. Tripathy, S. K. Singh, A. Behera, U. K. Sahu and R. K. Patel, *J. Mol. Liq.*, 2020, **315**, 113743.

31 M. M. Bade, A. A. Dubale, D. F. Bebizuh and M. Atlabachew, *ACS Omega*, 2022, **7**, 18770–18779.

32 N. Sato, Y. Amano and M. Machida, *SN Appl. Sci.*, 2022, **4**, 315.

33 E. Papadopoulou, D. Moutousidis, C. Achelonoudis, S. Tsompanidis, C. Kyriakou-Tziamtzi, K. Chrissafis and D. N. Bikiaris, *Materials*, 2025, **18**, 2632.

34 X. Ma, Y. Li, Y. Du, S. Chen, Y. Bai, L. Li, C. Qi, P. Wu and S. Zhang, *Environ. Sci. Pollut. Res. Int.*, 2024, **31**, 24113–24128.

35 G. V. Demirci, M. T. Baig and A. Kayan, *Int. J. Biol. Macromol.*, 2024, **283**, 137950.

36 Z. Xie, W. Guan, F. Ji, Z. Song and Y. Zhao, *J. Chem.*, 2014, **2014**, 1–9.

37 I. Neme, G. Gonfa and C. Masi, *Results Mater.*, 2022, **15**, 100304.

38 M. Sevilla and A. B. Fuertes, *J. Colloid Interface Sci.*, 2012, **366**, 147–154.

39 A. Hadadi, A. Imessaoudene, J.-C. Bollinger, S. Cheikh, A. Manseri and L. Mouni, *J. Polym. Environ.*, 2023, **31**, 2983–2998.

40 S. S. Hemdan, *J. Fluoresc.*, 2023, **33**, 2489–2502.

41 H. Zhang, X. Song, J. Zhang, Y. Liu, H. Zhao, J. Hu and J. Zhao, *Bioresour. Technol.*, 2022, **350**, 126884.

42 S. Ihaddaden, D. Aberkane, A. Boukerroui and D. Robert, *J. Water Process Eng.*, 2022, **49**, 102952.

43 A. A. Dubale, B. Boroje, W. M. Fereja and W.-Q. Wang, *Chem. Eng. J. Adv.*, 2025, **24**, 100916.

44 E. Makhado, *Surf. Interfaces*, 2025, **56**, 105699.

45 M. S. Khan, M. Khalid and M. Shahid, *RSC Adv.*, 2021, **11**, 2630–2642.

46 M. Moheb, A. M. El-Wakil and F. S. Awad, *RSC Adv.*, 2025, **15**, 674–687.

47 M. V. Nguyen, H. N. Nguyen, T. A. T. Nguyen and K. M. V. Nguyen, *RSC Adv.*, 2022, **12**, 30201–30212.

48 S. A. Aijaz, Z. Shafi and M. Shahid, *RSC Adv.*, 2025, **16**, 758–777.

49 A. Hajighasemkhan, L. Taghavi, E. Moniri, A. H. Hassani and H. A. Panahi, *Int. J. Environ. Anal. Chem.*, 2020, **102**, 1171–1191.

50 M. T. Baig and A. Kayan, *Int. J. Biol. Macromol.*, 2024, **280**, 135676.

51 K. Sunday and E. I. Amarachi, *J. Chem. Eng. Process Technol.*, 2025, **16**, 1000524.

52 K. V. Kumar, V. Ramamurthi and S. Sivanesan, *J. Colloid Interface Sci.*, 2005, **284**, 14–21.

53 H. Li, L. Liu, J. Cui, J. Cui, F. Wang and F. Zhang, *RSC Adv.*, 2020, **10**, 14262–14273.

54 M. T. Yagub, T. K. Sen and H. M. Ang, *Water, Air, Soil Pollut.*, 2012, **223**, 5267–5282.

55 V. Ponnusami, V. Gunasekar and S. N. Srivastava, *J. Hazard. Mater.*, 2009, **169**, 119–127.

56 X. Han, W. Wang and X. Ma, *Chem. Eng. J.*, 2011, **171**, 1–8.

57 J. Bortoluz, F. Ferrarini, L. R. Bonetto, J. da Silva Crespo and M. Giovanela, *Cellulose*, 2020, **27**, 6445–6466.

58 S. Dey, P. Bhagat, J. Mohanta and B. Dey, *Eur. J. Adv. Chem. Res.*, 2022, **3**, 1–11.

59 S. Soni, P. K. Bajpai, J. Mittal and C. Arora, *J. Mol. Liq.*, 2020, **314**, 113642.

60 S. Elhady, M. Bassyouni, M. Z. Elshikhiby, M. Y. Saleh and M. H. Elzahar, *Appl. Water Sci.*, 2024, **14**, 159.

61 M. Alsuhybani, M. Aleid, R. Alzidan, K. Bin Bander and A. Alrehaili, *Heliyon*, 2024, **10**, e36731.

62 A. A. Hoseini, S. Farhadi, A. Zabardasti and F. Siadatnasab, *RSC Adv.*, 2020, **10**, 40005–40018.

63 O. A. Urucu, B. Garosi and R. A. Musah, *ACS Omega*, 2025, **10**, 1943–1953.

64 P. Yang, Y. Lu, H. Zhang, R. Li, X. Hu, A. Shahab, A. Y. Elnaggar, A. F. Alrefaei, M. H. AlmutairiI and E. Ali, *Environ. Technol. Innovation*, 2024, **33**, 103459.

65 N. Yuan, H. Cai, T. Liu, Q. Huang and X. Zhang, *Adsorpt. Sci. Technol.*, 2019, **37**, 333–348.

66 D. Mekuria, A. Diro, F. Melak, T. G. Asere and R. Rehman, *J. Chem.*, 2022, **2022**, 1–13.

67 N. N. Mzinyane, *Heliyon*, 2024, **10**, e40071.

68 C. O. Aniagor, A. A. Aly, L. A. Mohamed and A. Hashem, *Waste Manage. Bull.*, 2024, **2**, 213–225.

69 A. H. Jawad, N. N. M. F. Hum, A. M. Farhan and M. S. Mastuli, *Desalin. Water Treat.*, 2020, **190**, 322–330.